Noname manuscript No.
(will be inserted by the editor)

Effects of Glia in a Triphasic Continuum Model of Cortical Spreading Depression

Rosemary O'Connell · Yoichiro Mori

Abstract Cortical spreading depression (SD) is a spreading disruption in brain ionic homeostasis during which neurons experience complete and prolonged depolarizations. SD is generally believed to be the physiological substrate of migraine aura and is associated with many other brain pathologies. Here, we perform simulations with a model of SD treating brain tissue as a triphasic continuum of neurons, glia and the extracellular space. A thermodynamically consistent incorporation of the major biophysical effects, including ionic electrodiffusion and osmotic water flow, allow for the computation of important physiological variables including the extracellular voltage (DC) shift. A systematic parameter study reveals that glia can act as both a disperser and buffer of potassium in SD propagation. Furthermore, we show that the timing of the DC shift with respect to extracellular K^+ rise is highly dependent on glial parameters, a result with implications for the identification of the propagating mechanism of SD.

Keywords cortical spreading depression · migraine · glia · potassium

Mathematics Subject Classification (2000) 92C50 · 92C30 · 35Q92

1 Introduction

Cortical spreading depression (SD) is a disorder of the central nervous system in which a population of brain cells experience complete depolarization, associated with a massive redistribution of ionic concentrations across the cell membrane (Charles and Brennan (2009); Dreier (2011); Somjen (2004)). This disturbance spreads at speeds of 2 to 7 mm/min. SD is widely accepted to be the physiological substrate of migraine aura (Dahlem and Hadjikhani (2009);

R. O'Connell · Y. Mori
School of Mathematics, University of Minnesota,
206 Church St SE, Minneapolis, MN 55455
E-mail: ymori@umn.edu

Hadjikhani et al (2001); Lashley (1941); Lehmenkühler and Aitken (1993); Tfelt-Hansen (2009)), and also plays a significant role in epilepsy, brain injury, cerebral ischemia, and stroke (Lauritzen et al (2010); Somjen (2004)). A fuller understanding of SD should thus lead to a better understanding of these clinical conditions. An understanding of SD should also provide insights into the homeostatic control of the brain ionic environment, and therefore into the workings of the central nervous system (Miura et al (2007); Somjen (2004)). Since its discovery by Leão 70 years ago (Leao (1944)), SD has been a subject of continuous experimental and theoretical study, with recent reviews by Charles and Brennan (2009); Dreier and Reiffurth (2015); Gorji et al (2001); Miura et al (2007); Pietrobon and Moskowitz (2014); Somjen (2004); Tfelt-Hansen (2009); Zandt et al (2015).

Despite sustained efforts, many fundamental questions remain unanswered. One of the difficulties lies in the fact that several different biophysical responses at different spatiotemporal scales take place concurrently during SD.

In this paper, we develop a model of SD that incorporates a full glial compartment in addition to the neuronal and extracellular. To the best of our knowledge, this is the first computational model in which the three major tissue compartments are treated on an equal footing. Our present work builds upon previous work in Mori (2015) in which we developed a theoretical framework for incorporating electrodiffusive and osmotic effects in the study of tissue-level electrophysiological phenomena, and presented preliminary SD simulations in a two-compartment model.

Mathematically, our model consists of a system of coupled partial differential algebraic equations governing the dynamics of ionic concentrations, voltage and volume fractions in the neuronal, extracellular and glial compartments. The system of equations are computationally solved in one spatial dimension to study SD propagation. An important feature of this computation is that we can more reliably compute the shift in extracellular voltage, or DC shift. The DC shift is one of the primary quantities measured in SD experiments, and its computation has been a longstanding unresolved issue (Mori (2015); Zandt et al (2015)). As we shall see, the DC shift is profoundly influenced by the presence of the glial compartment.

A full glial compartment allows for the assessment of the subtle role glia play in SD. The glial syncytium is widely thought to act as a K^+ buffer, or a sink that removes extracellular K^+, which may prevent or slow down SD (Largo et al (1997); Somjen (2004); Theis et al (2003)). It has, however, also been suggested that the glial syncytium may facilitate SD by "broadcasting" increased K^+ concentration to distant sites (Amzica et al (2002); Somjen (2004)).

Three glial parameters: Na^+/K^+ ATPase strength, K^+ channel density, and gap junctional coupling strength are varied systematically and their effects on SD propagation are examined. Increased Na^+/K^+ ATPase strength leads to slower propagation. The effect of the latter two parameters on propagation speed indicates that the balance of two parameters determines whether the glial compartment acts as a sink or disperser of K^+; for example, an increase

in glial gap junctional coupling strength leads to higher propagation speeds. We find, however, that a further increase in gap junctional coupling strength leads to propagation failure.

We also find that the relative timing of the extracellular K^+ concentration ($[K^+]_e$) rise and DC shift is greatly affected by glial parameters. This observation is of interest as it pertains to the following controversy on the mechanism of SD propagation. The most influential hypothesis for SD propagation is due to Grafstein (Grafstein (1956)), which posits that $[K^+]_e$ is the propagative agent. The SD waves simulated in this paper propagate via extracellular ionic diffusion, and is thus supportive of the Grafstein hypothesis. The main argument against the Grafstein hypothesis has been that the DC shift can often be observed prior to the steep rise in $[K^+]_e$ (Herreras et al (2005); Pietrobon and Moskowitz (2014)); this observation has been interpreted as an absence in a "prodromal rise" in $[K^+]_e$, leading to the suggestion that the extracellular spread of K^+ is not the propagating mechanism. We find, however, that when glial gap junctional coupling is high, the DC shift can indeed be seen prior to the rise in $[K^+]_e$, indicating that the absence of a "prodromal rise" of $[K^+]_e$ does not provide grounds to argue against the Grafstein hypothesis.

2 Mathematical Model

In this paper, nervous tissue is modeled as a homogenized continuum in which the three compartments, neuronal, glial and extracellular, overlap everywhere in space. Continuum modeling of nervous tissue is a common feature of SD models (Chang et al (2013); Dahlem and Chronicle (2004); Dahlem et al (2010); Nicholson (1993); Revett et al (1998); Tuckwell (1981); Tuckwell and Miura (1978); Yao et al (2011)). Most treat nervous tissue as a *bi*phasic continuum of neurons and extracellular space (ECS) only; in such models, the effect of glia is often incorporated as a sink or source term in the equations for extracellular ionic concentrations. In addition, all of the models cited above use the diffusion equation for ionic concentration, neglecting *electro*diffusive effects. The large changes in ionic concentration and cell volume during SD necessitates a model that incorporates ionic electrodiffusion and osmotic water flow in a physically consistent fashion. Indeed, during SD, extracellular K^+ concentration, for example, can rise from 5mmol/l to 50mmol/l. Such a significant local rise in K^+ concentration must be accompanied by a concomitant movement in other ions (most importantly Na^+ and Cl^-) to maintain electroneutrality of the bulk solution. Pure diffusion modeling of ionic concentrations in SD, therefore, leads to a significant violation of electroneutrality.

In our model, the theoretical foundation of which was established in Mori (2015), ionic concentrations obey the electrodiffusion equation with source terms corresponding to transmembrane fluxes. Transmembrane osmotic pressure differences drive transmembrane water flow thereby changing volume fraction. The voltage in each compartment is then determined by the electroneutrality condition (the charge-capacitance relation, to be precise, see (8)

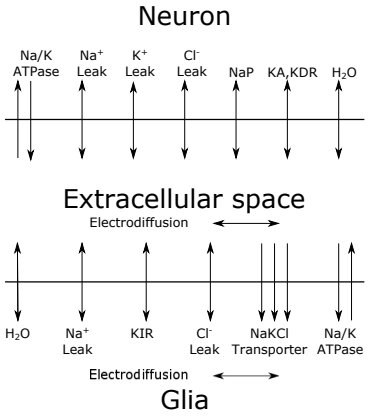

Fig. 1 Schematic diagram of the model.

and (10)). There are studies in which electrodiffusion is considered to varying degrees of completeness (Almeida et al (2004); Shapiro (2001)), but previous treatments have been flawed in their computation of the voltage, leading to a violation of electroneutrality. In addition, they cannot take into account electrotonic effects which are always present with (neuronal or glial) gap junctional coupling. In Mori (2015), it was found that the proper incorporation of electrotonic effects, made possible by our modeling framework, leads to unphysiologically fast SD propagation under significant neuronal gap junctional coupling, in direct contradiction with Shapiro (2001). An important added benefit of our modeling framework is that the extracellular voltage deflection, or the DC shift, is naturally computed as an output of the simulations. The DC shift, as noted previously, is an important measurement modality in SD. Computation of the DC shift has been reported in Almeida et al (2004), but its computation is physically inconsistent as discussed in Mori (2015).

An important feature of our modeling framework is that it is thermodynamically consistent in the sense that the model satisfies an appropriate free energy identity. This seemingly natural requirement of internal consistency is not (indeed *cannot*) be satisfied by any of the purely diffusive continuum models nor is it satisfied by previous electrodiffusive models. This free-energetic structure is respected in the development of the numerical scheme Mori (2015). Figure 1 shows a schematic diagram of the model.

The main new feature of the current paper with respect to our previous effort in Mori (2015) is that we have the glial compartment. As mentioned earlier, ours seems to be the first tri-phasic model, even with respect to purely diffusive continuum models. Incorporation of the glial compartment requires a host of membrane current models associated with the glial membrane. The parameters in these models must then be adjusted to yield reasonable steady states.

We now turn to a description of our equations. The presentation here largely follows Mori (2015). Nervous tissue of interest consists of three com-

partments, neuronal, glial, and extracellular, which we label by $k = \mathrm{n}$, g, e respectively. At each point in space, we track the volume fraction α_k, voltage ϕ_k, and ionic concentrations c_i^k, where the index i labels the ionic species. Here, we track the three major ionic species, Na^+, K^+, and Cl^-. The volume fractions α_k satisfy the relation $\sum_{k=\mathrm{n,g,e}} \alpha_k = 1$ and obey the following equations:

$$\frac{\partial \alpha_\mathrm{n}}{\partial t} = -\gamma_\mathrm{n} w_\mathrm{n}, \tag{1}$$

$$\frac{\partial \alpha_\mathrm{g}}{\partial t} = -\gamma_\mathrm{g} w_\mathrm{g}, \tag{2}$$

$$\frac{\partial \alpha_\mathrm{e}}{\partial t} = \gamma_\mathrm{n} w_\mathrm{n} + \gamma_\mathrm{g} w_\mathrm{g}, \tag{3}$$

where $\gamma_k, k = \mathrm{n}, \mathrm{g}$ is the area of cell membrane per unit volume of membrane k (the membrane separating the k-th compartment and the ECS), and $w_k, k = \mathrm{n}, \mathrm{g}$ denotes the transmembrane water flow per unit area of the same membrane. The concentrations c_i^k satisfy the following equations.

$$\frac{\partial (\alpha_\mathrm{n} c_i^\mathrm{n})}{\partial t} = -\nabla \cdot \mathbf{f}_i^\mathrm{n} - \gamma_\mathrm{n} j_i^\mathrm{n}, \tag{4}$$

$$\frac{\partial (\alpha_\mathrm{g} c_i^\mathrm{g})}{\partial t} = -\nabla \cdot \mathbf{f}_i^\mathrm{g} - \gamma_\mathrm{g} j_i^\mathrm{g}, \tag{5}$$

$$\frac{\partial (\alpha_\mathrm{e} c_i^\mathrm{e})}{\partial t} = -\nabla \cdot \mathbf{f}_i^\mathrm{e} + \gamma_\mathrm{n} j_i^\mathrm{n} + \gamma_\mathrm{g} j_i^\mathrm{g}, \tag{6}$$

where

$$\mathbf{f}_i^k = -D_i^k \left(\nabla c_i^k + \frac{z_i F c_i^k}{RT} \nabla \phi_k \right), \tag{7}$$

Here, D_i^k is the diffusion coefficient of the i-th ion in the k-th compartment, z_i is the valence ($+1$ for Na^+ and K^+, -1 for Cl^-) and R, T, and F are the ideal gas constant, absolute temperature, and Faraday's constant. The source terms $j_i^k, k = \mathrm{n}, \mathrm{g}$ are the transmembrane ion fluxes per unit membrane area, the specific form of which is discussed below. In the ECS, D_i^k is proportional to the volume fraction, and in the neuronal and glial compartments, D_i^k expresses the strength of gap junctional coupling. The above equations are supplemented by the following charge-capacitance relations.

$$\gamma_\mathrm{n} C_\mathrm{m}^\mathrm{n} \phi_\mathrm{ne} = \rho_0^\mathrm{n} + \sum_{i=1}^{M} z_i F \alpha_\mathrm{n} c_i^\mathrm{n}, \tag{8}$$

$$\gamma_\mathrm{g} C_\mathrm{m}^\mathrm{g} \phi_\mathrm{ge} = \rho_0^\mathrm{g} + \sum_{i=1}^{M} z_i F \alpha_\mathrm{g} c_i^\mathrm{g}, \tag{9}$$

$$-\gamma_\mathrm{n} C_\mathrm{m}^\mathrm{n} \phi_\mathrm{ne} - \gamma_\mathrm{g} C_\mathrm{m}^\mathrm{g} \phi_\mathrm{ge} = \rho_0^\mathrm{e} + \sum_{i=1}^{M} z_i F \alpha_\mathrm{e} c_i^\mathrm{e}. \tag{10}$$

Here C_{m}^k is the membrane capacitance per unit area of membrane k, $\phi_{k\mathrm{e}} = \phi_k - \phi_{\mathrm{e}}$ denotes the membrane potential, and ρ_0^k is the charge density contributed by the immobile ions in the k-th compartment. As is well-known, the charge stored on the capacitive membrane is very small compared to the absolute amount of charge in the bulk; that is to say, the capacitances C_{m} are typically "small" in sense that can be made precise by a non-dimensionalization Mori (2015). Hence, the above charge-capacitance relation ensures (near) electroneutrality of each of the compartments. Eq. 1–10 comprise a partial differential algebraic system of 15 equations in 15 unknowns (α_k, ϕ_k, and the three ionic concentrations c_i^k, in each of the three compartments).

The constitutive relation for water flux w_k and ionic flux j_i^k for $k = \mathrm{n}, \mathrm{g}$ are given as follows:

$$w_k = \eta_k RT \left(\frac{a_{\mathrm{e}}}{\alpha_{\mathrm{e}}} + \sum_{i=1}^{M} c_i^{\mathrm{e}} - \frac{a_k}{\alpha_k} - \sum_{i=1}^{M} c_i^k \right), \ k = \mathrm{n}, \mathrm{g} \tag{11}$$

$$j_i^k = h_i^k + \sum_m \hat{g}_i^{k,m} J_i^{k,m}, \ k = \mathrm{n}, \mathrm{g}. \tag{12}$$

The water flux is proportional to the osmotic pressure, with η_k the hydraulic permeability of membrane k and a_k the amount of immobile ions in compartment k. The ionic flux is a combination of flow due to ion pumps and cotransporters, h_i^k, and various ion channels. Each channel flux is given as the product of $\hat{g}_i^{k,m}$, the proportion of open channels, and the flux-voltage-concentration relationship $J_i^{k,m}$. The functions $\hat{g}_i^{k,m}$ are in turn often functions of gating variables whose dynamics is governed by their own set of ordinary differential equations.

For the neuronal membrane channels, we use the persistent sodium channel (NaP), the potassium delayed rectifier (KDR), the transient potassium channel (KA), and $\mathrm{Na}^+/\mathrm{K}^+$ ATPase, as well as leak currents for each of Na^+, K^+, and Cl^-. The equations used for these channels are those of Kager et al (2000) and Yao et al (2011). For the glial membrane channels, we are unaware of a comprehensive list of channels that may be relevant to SD, and we collected an assortment of channels from different sources. In particular, we use the potassium inward rectifier (KIR) of Newman (1993); Steinberg et al (2005), the $\mathrm{Na}^+/\mathrm{K}^+$ ATPase of Yao et al (2011), and the sodium, potassium, and chloride (NaKCl) cotransporter of Bennett et al (2008). The leak currents for the glia are Na^+ and Cl^-, again using the equations of Kager et al (2000) and Yao et al (2011). Because of the disparate sources, it was necessary to adjust the permeabilities of some of the channels in order to maintain a reasonable rest state. The details of these changes are described below. The equations governing the ion channel models are available in the appendix.

Table 1 Steady state values

	Neuronal	Glial	Extracellular
α	0.5	0.3	0.2
$[Na^+]$ (mM)	10	10	140
$[K^+]$ (mM)	130	130	3.4
$[Cl^-]$ (mM)	7.2522*	7.2522*	120
ϕ (mV)	-75	-90	0
a (mmol)	59.3239*	35.5943*	.5
ρ_0 (C)	-6.4045×10^3*	-3.8429×10^3*	-0.4508×10^3*

Values with asterisks were calculated as described in section 2.1, while those without asterisks were chosen based on values in the literature.

We point out here the connection of Eq. 1–12 to cable theory. We may take the derivative of Eq. 8 in time and use Eq. 4 to obtain:

$$\begin{aligned} \gamma_k \left(C_{\mathrm{m}}^k \frac{\partial \phi_{k\mathrm{e}}}{\partial t} + I_k \right) &= \nabla \cdot (\mathbf{b}_k + a_k \nabla \phi_k), \ k = \mathrm{n}, \mathrm{g} \\ a_k = \sum_{i=1}^{3} D_i^k \frac{(z_i F)^2 c_i^k}{RT}, \ \mathbf{b}_k &= \sum_{i=1}^{3} z_i F D_i^k \nabla c_i^k. \end{aligned} \tag{13}$$

In much the same way, we obtain, from Eq. 10:

$$-\sum_{k=\mathrm{n,g}} \gamma_k \left(C_{\mathrm{m}}^{\mathrm{k}} \frac{\partial \phi_{k\mathrm{e}}}{\partial t} + I_k \right) = \nabla \cdot (\mathbf{b}_{\mathrm{e}} + a_{\mathrm{e}} \nabla \phi_{\mathrm{e}}), \tag{14}$$

where a_{e} and $\mathbf{b}_{\mathrm{e}}$ are as in (13). Under the assumption of spatially constant ionic concentrations, the above reduces to a cable-type equation. It is in this sense that electrotonic effects are included in the model. When there are only two compartments, what we have is essentially the bidomain model used extensively in cardiac electrophysiology Keener and Sneyd (1998). We do not, however, know of any significant study in tissue electrophysiology using a *tri*domain model, even outside of neural electrophysiology. As we shall see in Section 3.2, the electrotonic effects that arise from glial gap junctional coupling share some features seen in cardiac bidomain models but are otherwise quite subtle.

2.1 Initial and boundary conditions

SD is simulated in one spatial dimension with no-flux boundary conditions for all ions at both edges of the domain. For the majority of our simulations, the initial conditions and some of the ion channel parameters were chosen to ensure that the system was at a stationary state. For consistency in our results, we chose to have the same resting values for as many of our simulations as possible, which necessitated adjusting some of the parameter values from those given in the literature. As noted before, the inclusion of channels from different sources for the glial membrane contributed to the need to take care in

Table 2 Parameter values

Parameter	Value	Source
C_{m}	$0.75\ \mu\mathrm{F/cm^2}$	Kager et al (2000); Yao et al (2011)
$P^{\mathrm{n,P}}_{\mathrm{Na}}$	2×10^{-5} cm/s	Kager et al (2000); Yao et al (2011)
$P^{\mathrm{n,DR}}_{\mathrm{K}}$	1×10^{-3} cm/s	Kager et al (2000); Yao et al (2011)
$P^{\mathrm{n,A}}_{\mathrm{K}}$	1×10^{-4} cm/s	Kager et al (2000); Yao et al (2011)
$P^{\mathrm{g,IR}}_{\mathrm{K}}$	13×10^{-2} mS/cm^2	Steinberg et al (2005)
$P^{\mathrm{n,L}}_{\mathrm{Na}}$	5.1774×10^{-9} mmol/cm^2/s	calculated
$P^{\mathrm{g,L}}_{\mathrm{Na}}$	7.5693×10^{-10} mmol/cm^2/s	calculated
$P^{\mathrm{n,L}}_{\mathrm{K}}$	7×10^{-2} mS/cm^2	Yao et al (2011)
$P^{\mathrm{n,L}}_{\mathrm{Cl}}$	10×10^{-2} mS/cm^2	Kager et al (2000)
$P^{\mathrm{g,L}}_{\mathrm{Cl}}$	5×10^{-2} mS/cm^2	[a]
m_{K}	2×10^{-3} mmol/cm^3	Yao et al (2011)
m_{Na}	7.7×10^{-3} mmol/cm^3	Yao et al (2011)
$\bar{I}_{\mathrm{n}}$	1.3299×10^{-7} mmol/cm^2/s	calculated
$\bar{I}_{\mathrm{g}}$	3.932×10^{-8} mmol/cm^2/s	calculated
P^{NaKCl}	8.4351×10^{-10} mmol/cm^2/s	calculated
η	5.4×10^{-5} cm/sec/(mmol/cm^3)	Shapiro (2000)
D^*_{Na}	1.33×10^{-5} cm^2/sec	Hille et al (2001)
D^*_{K}	1.96×10^{-5} cm^2/sec	Hille et al (2001)
D^*_{Cl}	2.03×10^{-5} cm^2/sec	Hille et al (2001)
γ_{n}	6.3849×10^3 1/cm	Kager et al (2000); Yao et al (2011)
γ_{g}	6.3849×10^3 1/cm	[b]
T	310.15 K	

[a] Glial Cl^- leak value chosen to ensure that other parameter values were always positive.
[b] Glial area of cell membrane per unit volume taken to be equal to that of the neuron.

setting parameters. We set the equilibrium values to be those given in Table 1, with the neuronal chlorine concentration dictated by the extracellular chlorine concentration and the membrane potential because chlorine only crossed the neuronal membrane through a leak channel in our model. We set the glial chlorine concentration equal to the neuronal chlorine concentration.

With the volume fraction, concentrations, and electrostatic potentials set, we determined the parameter values as necessary for the system to be at rest. In order to have $\frac{\partial c_i^k}{\partial t} = 0$, we must have the net flow of each ion across all channels equal to 0. For each cell type and ion type, we can set all but one permeability arbitrarily and solve for that, provided we ensure that all permeabilities are positive. Because of our focus on K^+, we set the values of channels involving K^+ first and set the Na^+ leak permeability last. Specifically, we start with the neuron by taking the KDR and KA permeability and gating variables and the leak permeability from Kager et al (2000) and Yao et al (2011)) and then set the Na^+/K^+ ATPase pump strength so that $\frac{\partial c^{\mathrm{n}}_{\mathrm{K}}}{\partial t} = 0$. We then took the NaP permeability and gating variables from the literature and set the Na^+ leak permeability so that $\frac{\partial c^{\mathrm{n}}_{\mathrm{Na}}}{\partial t} = 0$.

For the glial compartment, we first set the NaKCl cotransporter permeability so that the glial Cl^- concentration was at rest. We then set the KIR channel strength, either from the literature (Steinberg et al (2005)) or modified for experimental purposes, and calculated the glial Na^+/K^+ ATPase pump strength

so that $\frac{\partial c_{\mathrm{K}}^{\mathrm{g}}}{\partial t} = 0$. Since the only other Na^+ current on the glial membrane in our model is the leak current, we then set the Na^+ leak permeability so that $\frac{\partial c_{\mathrm{Na}}^{\mathrm{g}}}{\partial t} = 0$. We note that the glial Na^+/K^+ ATPase pump strength and leak Na^+ permeability were both dependent on the glial KIR strength. Values of all parameters are given in table 2.

Finally, to ensure that the volume fractions were at rest and the charge-capacitance relationships were properly satisfied, we set the organic (impermeable) anion amounts and the charge densities they contribute in each compartment. The extracellular organic anion amount was set arbitrarily, and the intracellular amounts were set so that the total osmotic pressure in all compartments was equal. The charge densities were set in each compartment independently so that the charge-capacitance relationships were satisfied. These values are given in table 1.

For the simulations in which the Na^+/K^+ ATPase strength was varied, the adjustment was made after all parameter values were set as above by multiplying $\bar{I}$, the maximum pump strength, by a constant. The change resulted in the initial condition no longer being a rest state, and the simulation was allowed to approach a rest state prior to introducing the excitatory fluxes that triggered SD. Table 3 shows the resulting rest state values for these simulations.

The diffusion coefficients were calculated differently for each compartment. The neuronal diffusion coefficients were all set to 0. The glial diffusion coefficients were assumed to be independent of volume changes, since diffusion in the glial compartment was assumed to occur through gap junctions, but the initial volume fraction of the glia was used in determining the coefficient. The extracellular diffusion coefficients were assumed to be proportional to the volume fraction.

$$\begin{aligned} D_i^{\mathrm{n}} &= 0, \\ D_i^{\mathrm{g}} &= D_i^* \alpha_{\mathrm{g}}^0, \\ D_i^{\mathrm{e}} &= D_i^* \alpha_{\mathrm{e}}. \end{aligned}$$

In all cases, SD was triggered by adding excitatory transmembrane fluxes for all ions to the neuronal compartment at the left-most point, similar to that of Mori (2015). The excitatory fluxes were of the form

$$j_{iE} = G_E(t,x)\left(z_i F \phi_{\mathrm{ne}} - RT \ln\left(\frac{c_i^{\mathrm{e}}}{c_i^{\mathrm{n}}}\right)\right), \tag{15}$$

$$G_E(t,x) = \begin{cases} G_{max}\cos^2(\pi x/(2x_E))\sin(\pi t/t_E) & \text{if } 0 \le x < x_E \text{ and } 0 \le t \le t_E, \\ 0 \quad \text{otherwise.} \end{cases} \tag{16}$$

We set $x_E = \triangle x$, $t_E = 2$ s, and $G_{max}F^2 = 0.5$ mS/cm^2, where $\triangle x = 20\mu$m is the spatial discretization size as described in Section 2.2. The excitatory fluxes result in a nonselective membrane conductance that opens at the left edge for two seconds. Other methods of triggering SD, such as increasing the

Table 3 Rest values for different Na^+/K^+ ATPase values, with b_n and b_g denoting the multiplier for the neuronal and glial membranes. All concentrations are in mM and potentials in mV. For all values, we have $\alpha_e = 1 - \alpha_n - \alpha_g$ and $\phi_e = 0$.

b_n	b_g	α_n	α_g	c^n_{Na}	c^g_{Na}	c^e_{Na}	c^n_K	c^g_K	c^e_K	c^n_{Cl}	c^g_{Cl}	c^e_{Cl}	ϕ_n	ϕ_g
0.7	0.7	0.5065	0.3027	11.62	11.4	139.73	128.29	128.54	4.17	8.86	8.37	119.38	-69.51	-85.35
0.8	0.8	0.5035	0.3016	10.90	10.83	139.81	129.05	129.13	3.86	8.14	7.92	119.66	-71.85	-87.14
0.9	0.9	0.5015	0.3007	10.4	10.38	139.91	129.58	129.61	3.61	7.64	7.56	119.85	-73.59	-88.66
1	1	0.5	0.3	10	10	140	130	130	3.4	7.25	7.25	120	-75	-90
1.1	1.1	0.4988	0.2994	9.67	9.68	140.08	130.34	130.33	3.22	6.95	6.99	120.12	-76.18	-91.19
1.2	1.2	0.4978	0.2988	9.40	9.41	140.16	130.63	130.61	3.07	6.69	6.76	120.22	-77.19	-92.26
1.3	1.3	0.4969	0.2983	9.16	9.18	140.23	130.88	130.86	2.93	6.48	6.55	120.30	-78.08	-93.23
1.4	1.4	0.4962	0.2979	8.96	8.97	140.29	131.10	131.08	2.81	6.29	6.37	120.37	-78.81	-94.11
1	0.5	0.5061	0.3021	9.20	14.99	139.77	130.71	124.96	4.07	8.76	8.11	119.45	-69.82	-85.52
1	0.6	0.5039	0.3104	9.39	13.41	139.82	130.56	126.56	3.86	8.22	7.93	119.65	-71.57	-86.91
1	0.7	0.5024	0.3009	9.57	12.24	139.88	130.40	127.74	3.70	7.86	7.62	119.78	-72.79	-87.96
1	0.8	0.5014	0.3005	9.73	11.33	139.92	130.25	128.65	3.58	7.61	7.47	119.87	-73.70	-88.79
1	0.9	0.5006	0.3002	9.87	10.60	139.96	130.12	129.39	3.48	7.41	7.35	119.95	-74.42	-89.45
1	1.1	0.4995	0.2998	10.11	9.49	140.03	129.89	130.51	3.33	7.13	7.18	120.04	-75.48	-90.46
1	1.2	0.4991	0.2997	10.22	9.05	140.06	129.80	130.95	3.28	7.02	7.11	120.08	-75.89	-90.85
1	1.3	0.4987	0.2995	10.31	8.68	140.08	129.71	131.34	3.23	6.93	7.06	120.11	-76.24	-91.19
1	1.4	0.4984	0.2994	10.39	8.34	140.11	129.63	131.67	3.18	6.85	7.01	120.14	-76.55	-91.49
1	1.5	0.4981	0.2993	10.47	8.05	140.13	129.56	131.97	3.15	6.78	6.97	120.16	-76.82	-91.75

extracellular K^+ and Cl^- concentrations, would require modeling the external source in detail to maintain the biophysical consistency of the system. Adding excitatory fluxes in this manner is simpler and may well be one of the mechanisms by which SD occurs naturally. The specific form of the excitation conductance was selected because it is continuous, matching the continuity of the system, and has compact support, allowing the excitation to end and making full recovery to the initial resting values possible.

2.2 Numerical computation

Eq. 1–12 comprise a numerically stiff system of partial differential algebraic equations with disparate time scales including the slow electrodiffusive/osmotic time scales and the fast electrotonic/channel gating time scales. Simulations were run in Matlab®. We give a brief account of the numerical algorithm and refer the reader to Mori (2015) (in which a biphasic version of this algorithm is implemented) for details. One temporal step is divided into two substeps. In the first substep, the ionic concentrations c_i^k, volume fractions α_k and the voltages ϕ_k are updated. In the second substep, the gating variables of the neuronal and glial ion channels are updated, a relatively simple procedure since the gating variables are governed by pointwise ODEs. We now describe the first substep, which represents the bulk of the computational work. We use a finite volume discretization in space reflecting the divergence structure of the model system. There are disparate time scales of importance in our system including the electrotonic and electrodiffusive, which necessitates an implicit time discretization to ensure stability. Let $\triangle x$ and $\triangle t$ be the width of our spatial and temporal discretizations, respectively, and let $y_{k,l}^n$ approximate y_k at $x = l\triangle x$ and $t = n\triangle t$, where y represents any of our dependent variables. For notational simplicity, we let $\mathcal{D}_x^+(y_{k,l}^n) = \frac{1}{\triangle x}(y_{k,l+1}^n - y_{k,l}^n)$, $\mathcal{D}_x^-(y_{k,l}^n) = \frac{1}{\triangle x}(y_{k,l}^n - y_{k,l-1}^n)$, and $\mathcal{D}_t^-(y_{k,l}^n) = \frac{1}{\triangle t}(y_{k,l}^n - y_{k,l}^{n-1})$ denote our

difference operators. With this notation, our discretized equations are:

$$\mathcal{D}_t^-(\alpha_{k,l}^n) = -\gamma_k w_{k,l}^n,\ k = \mathrm{n}, \mathrm{g}, \quad \alpha_{\mathrm{n},l}^n + \alpha_{\mathrm{g},l}^n + \alpha_{\mathrm{e},l}^n = 1, \tag{17}$$

$$w_{k,l}^n = \eta_k RT \left(\frac{a_{\mathrm{e},l}}{\alpha_{\mathrm{e},l}^n} - \frac{a_{k,l}}{\alpha_{k,l}^n} + \sum_{i=1}^{M} (c_{i,l}^{\mathrm{e},n} - c_{i,l}^{k,n}) \right), \tag{18}$$

$$\mathcal{D}_t^-(\alpha_{k,l}^n c_{i,l}^{k,n}) = -\mathcal{D}_x^-(\mathbf{f}_{i,l}^{k,n}) - \gamma_k j_{i,l}^{k,n},\ k = \mathrm{n}, \mathrm{g}, \tag{19}$$

$$\mathcal{D}_t^-(\alpha_{\mathrm{e},l}^n c_{i,l}^{\mathrm{e},n}) = -\mathcal{D}_x^-(\mathbf{f}_{i,l}^{\mathrm{e},n}) + \gamma_{\mathrm{n}} j_{i,l}^{\mathrm{n},n} + \gamma_{\mathrm{g}} j_{i,l}^{\mathrm{g},n}, \tag{20}$$

$$\mathbf{f}_{i,l}^{k,n} = -D_i^k(\alpha_{k,l}^{n-1}) \left(\frac{c_{i,l+1}^{k,n-1} + c_{i,l}^{k,n-1}}{2} \right) \mathcal{D}_x^+ \left(\ln(c_{i,l}^{k,n}) + \frac{z_i F}{RT} \phi_{k,l}^n \right), \tag{21}$$

$$j_{i,l}^{k,n} = h_{i,l}^{k,n-1} + \sum_m \hat{g}_{i,l}^{k,m,n-1} J_{i,l}^{k,m,n}, \tag{22}$$

$$\gamma_k C_{\mathrm{m}}^k \phi_{\mathrm{ke},l}^n = \rho_0^k + \sum_{i=1}^{3} z_i F \alpha_{k,l}^n c_{i,l}^{k,n},\ k = \mathrm{n}, \mathrm{g}, \tag{23}$$

$$-\gamma_{\mathrm{n}} C_{\mathrm{m}}^{\mathrm{n}} \phi_{\mathrm{ne},l}^n - \gamma_{\mathrm{g}} C_{\mathrm{m}}^{\mathrm{g}} \phi_{\mathrm{ge},l}^n = \rho_0^{\mathrm{e}} + \sum_{i=1}^{3} z_i F \alpha_{\mathrm{e},l}^n c_{i,l}^{\mathrm{e},n}. \tag{24}$$

The resulting system of nonlinear algebraic equations is solved using a Newton iteration.

3 Results

We examined the effects of varying several parameters controlling the behavior of K^+ in the glial compartment, paying particular attention to the speed of propagation and relative timing of various aspects of SD. Our simulations covered a domain 1 cm wide, with SD triggered at the left edge. To measure the speed of propagation, we set a threshold of 10 mV and recorded when the change in the neuronal membrane potential reached the threshold at each point in our discretization. After restricting our attention to the points between 2.5 and 7.5 mm from the edge to ensure edge effects did not affect the calculation, we used linear regression to determine the speed of propagation. In all cases, the R^2 value was within 10^{-7} of 1.

In order to study the relationship in the timing, we chose thresholds of a change in 2 mV from the resting values for the extracellular potential and the membrane potentials and of 1 mM in $[K^+]_{\mathrm{e}}$. We recorded the times at which these thresholds were reached at 5 mm, taking $t = 0$ to be the starting time for SD at 2.5 mm.

3.1 General Results

The general shape of the simulated wave was similar to experimentally recorded traces, featuring a DC shift, ionic concentration changes, and cell swelling as

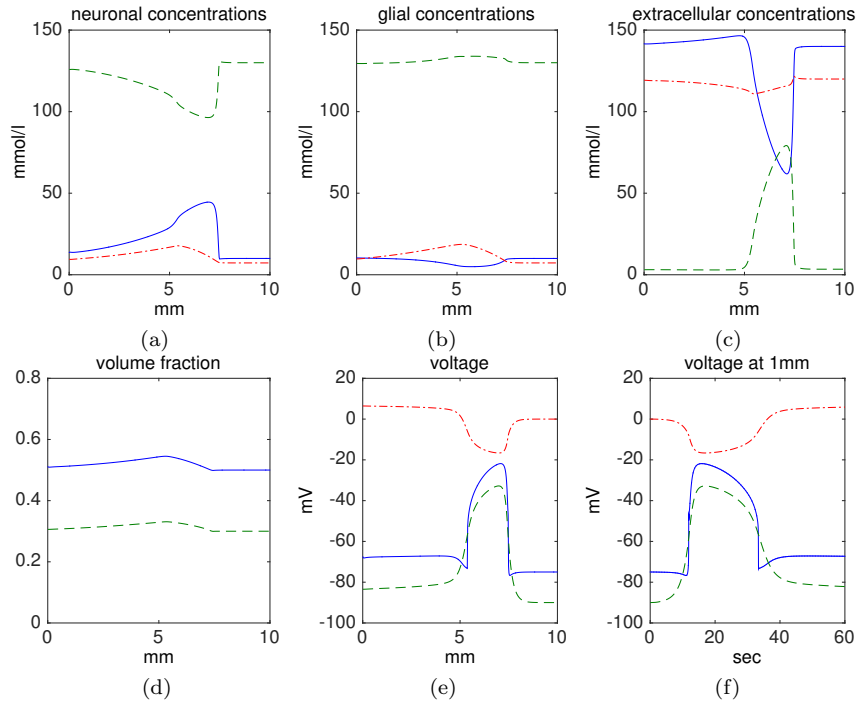

Fig. 2 Sample simulation of SD with glial gap junction strength $d = 0.25$ and potassium conductance strength $a = 2$, with a snapshot after about 78 seconds of simulated time shown in (a)–(e) and a trace in time at 1 mm in (f). Concentrations of Na^+ (solid), K^+ (dashed) and Cl^- (dashed dotted) are shown for the neurons (a), glia (b), and ECS (c). The volume fractions for neurons (solid) and glia (dashed) are shown in (d), and voltages for neurons (solid), glia (dashed), and the ECS (dashed dotted) are shown in (e) and (f).

shown in Fig. 2. The propagation speeds were also near experimentally observed speeds of 1–15 mm/min (Miura et al (2007)), falling in the range of 4–9 mm/min, with the majority of the simulations between 4 and 6 mm/min. All of our simulations showed a positive tail to the DC shift after the initial negative shift, a feature present in many experiments (Canals et al (2005); Gorji et al (2001); Herreras and Somjen (1993); Lehmenkühler (1990); Richter and Lehmenkühler (2008); Sugaya et al (1975)). A similar undershoot in $[K^+]_e$ occurred in our simulations, typically dropping past the resting value of 3.4 mM to a minimum of 2.9 mM before recovering, which was also evident in some experiments (Gorji et al (2001); Lehmenkühler (1990); Richter and Lehmenkühler (2008)).

To see the effect of adding the glial compartment, we compare our results with a simulation without a glial compartment. In this two-compartment simulation, the volume fraction of the neuronal compartment is 0.8 and all other initial conditions and parameters are set as described in section 2.1, with a snapshot shown in Fig. 3. Aside from the initial conditions and a few param-

eter values, this simulation is identical to the simulations in Mori (2015). The overall form of many of the neuronal and extracellular variables are not significantly affected with the addition of the glial compartment. The neuronal ionic concentrations, voltage, and volume changes and the extracellular ionic concentration and volume change remain similar. This overall similarity implies that SD propagation in our model is due primarily to extracellular ionic (electro)diffusion, lending support to the Grafstein hypothesis. Indeed, in the two-compartment model, the extracellular ionic (electro)diffusion is the only mechanism by which propagation can take place since neuronal gap-junctional coupling is set to 0 (see equation (15)). The extracellular concentrations, however, does show a reduction in magnitude with the glial compartment, in line with the view that the glia should be acting as a buffer. This reduction in magnitude includes the undershoot of $[K^+]_e$ after the SD wave.

The most prominent difference is that the extracellular voltage deflection, or the DC shift, is much larger, which is in better correspondence with experimentally observed values. As can be seen from Fig. 2 (see also Fig. 4a), an early and gradual DC shift precedes the rapid change in neuronal voltage or $[K^+]_e$, and such an early DC shift is absent in Fig. 3. Fig. 2 also shows a small positive tail in the DC shift following the negative shift, which is a feature that was not significant in the simulation without a glial compartment. The DC shift is highly affected by changes to parameters in the glial compartment, and this dependence will be studied in detail below.

The glial concentrations of Na^+ and K^+ deflect in the same direction as the extracellular space, with a smaller magnitude, reflecting the buffering capacity of glia. The glial Cl^- concentration, however, deflects in the opposite direction reflecting a net accumulation of ions. This leads to osmotic swelling of the glial compartment. Glia also exhibit a depolarization similar to neurons, again in line with experimental data (Sugaya et al (1975)), which is slightly larger in magnitude though the glia remain at a lower potential than the neurons.

3.2 Glial Gap Junctions and K^+ Channel Density

To study how glial K^+ handling affects SD, we vary glial gap junctional coupling and the density of inward-rectifying K^+ channels on the glial membrane and study their effects on the SD wave. Glial gap junctional coupling is reflected in the glial diffusion coefficient. The diffusion coefficients for all ions in the glial compartment were adjusted by factor d, which we shall refer to as the gap junction strength:

$$D_i^{\mathrm{g}} = dD_i^* \alpha_{\mathrm{g}}^0,$$

where D_i^* is the diffusion coefficient in water and α_{g}^0 is the initial volume fraction of the glial compartment. Likewise, the density of inward-rectifying K^+ channels is varied by multiplying the reference value with a factor a, which we shall call the glial K^+ conductance strength.

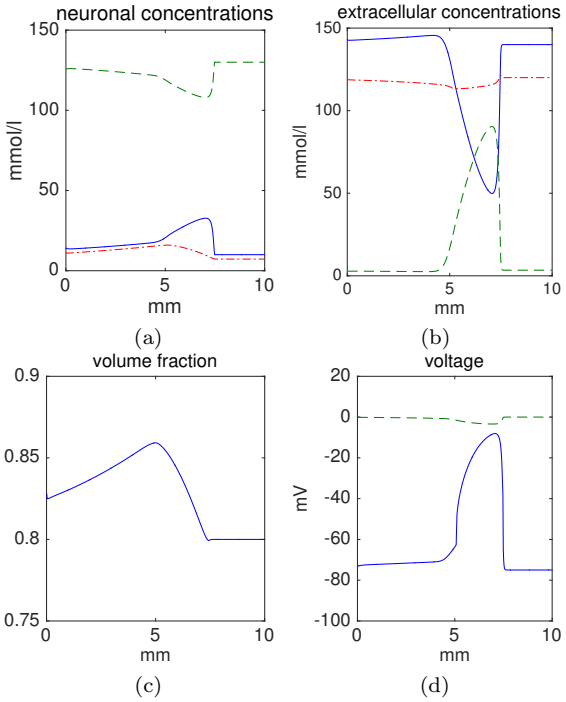

Fig. 3 Sample simulation of SD without a glial compartment after about 86 seconds of simulated time. Concentrations of Na^+ (solid), K^+ (dashed) and Cl^- (dashed dotted) are shown for the neurons (a) and ECS (b). The volume fraction of the neuronal compartment is shown in (c), and voltages for neurons (solid) and the ECS (dashed) are in (d).

DC shift Snapshots of the DC shift for different values of gap junctional coupling d with $a = 2$ are shown in Fig. 4a. The magnitude of the DC shift in the ECS increased with increasing gap junctional coupling in the glial compartment, but was minimally affected by the glial K^+ conductance (not shown). For values of d less than $d = 0.03$, the DC shift was around 3 to 5 mV. From there, increases in d causes noticeable increases in the DC shift, with values around 10 mV when $d = 0.125$, 16 mV when $d = 0.25$, and 25 mV when $d = 0.5$. Fig. 4a also shows a greater early deflection in the DC shift with increased d, as well as a positive overshoot for higher values of d.

The DC shift can be understood as being composed of two components, the diffusive and the electrotonic. For $d = 0$ or small values of d, the DC shift is primarily a result of the diffusion potential created by the concentration gradients in the ECS. The DC shift in the two-compartment simulation as shown in Fig. 3 consists entirely of this diffusive component. For high values of gap junctional coupling, the DC shift consists primarily of the the electrotonic component. Increasing glial gap junctional coupling reduces electrical resistance in the glial syncytium, which allows for a larger voltage deflection through the ECS and a smaller deflection in the glia. When $d = 1$, the glial and

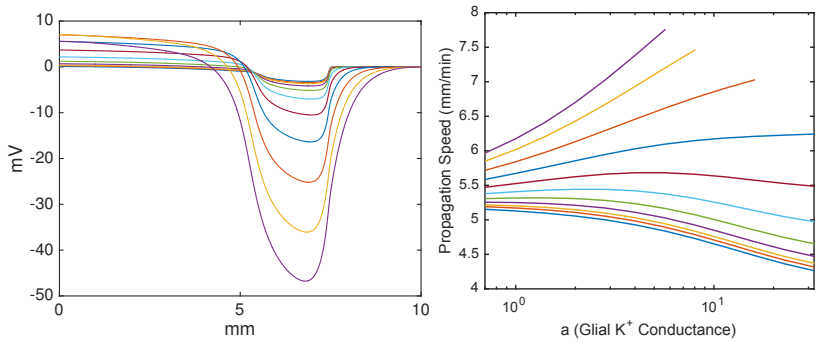

Fig. 4 Effects of glial gap junctional coupling and potassium conductance on the magnitude of the DC shift (a), and the propagation speed of SD (b). (a) DC shift at different values of the gap junctional coupling d with $a = 2$. The trace with the smallest DC shift in magnitude corresponds to $d = 0$ and the remaining lines show d equal to powers of 2 from 2^{-8} to 2. The magnitude of the DC shift at $d = 2$ is the greatest. (b) The lowest line shows $d = 0$ and the remaining lines show d equal to powers of 2 from 2^{-8} to 2. Both parameters affected the propagation speed, with lowest speeds corresponding to low gap junctional coupling and high potassium conductance and highest speeds corresponding to high gap junctional coupling and high potassium conductance. If a balance of both parameters was sufficiently high, propagation failed, corresponding to the cut off corner.

extracellular diffusion coefficients are the same, resulting in the voltage deflection being split nearly equally across the two compartments. In our model, the glial voltage goes up by 35.1 mV and the extracellular voltage drops by 36.2 mV when $d = 1$. As d decreases from 1, the change in voltage is increasingly limited to the glial compartment, resulting in smaller DC shifts. The early deflection of the DC shift for high values of d, as seen in Fig. 4a, is also due to the electrotonic spread of current. These results offer computational support for glial involvement in sustained potentials discussed in Somjen (1973), and are in agreement with the DC shift observed in mice with varying degrees of astrocyte-directed inactivation of gap junctions (Theis et al (2003)).

Speed The effects of the glial gap junction strength and the glial K^+ conductance strength on the propagation speed of SD are shown in Fig. 4b. For small values of the gap junction strength, increasing the K^+ conductance decreases the propagation speed. With small values for both of these parameters, speeds were similar to that of the simulation without glia, where propagation occurred at 5.2 mm/min. For large values of the gap junction strength, increasing the K^+ conductance increases the propagation speed. For intermediate values of the gap junction strength, the propagation speed shows biphasic behavior as a function of the K^+ conductance, attaining a maximum at an intermediate value of K^+ conductance. In all cases, increasing the gap junction strength with a constant K^+ conductance resulted in increasing propagation speed, though the rate of increase is higher for larger K^+ conductances. However, if

both the gap junction strength and the K^+ conductance strength were high, the SD event triggered at the left edge did not propagate through the domain, corresponding to the cut off of the traces in Fig. 4b. Values of d and a for which propagation failed were $(d, a) = (0.5, 22.6274)$, $(1, 11.3137)$, and $(2, 8)$, as well as all values for which one or both parameters were higher.

These results suggest a subtle role of glial cells in controlling $[K^+]_e$. The glia either buffer or broadcast K^+, depending on the values of the gap junction strength and the K^+ conductance strength. If the gap junction strength is low and the K^+ conductance is high, the glia act as a K^+ buffer as K^+ passes into the glial cells but is not released into the ECS elsewhere, resulting in a relatively low propagation speed. However, the glia broadcast K^+ if the gap junction strength is high but the K^+ conductance is low, with K^+ entering the glial cells leading to a release of K^+ in the ECS away from the SD event, which results in a faster speed of propagation. This seems to be the first computational support of K^+ broadcasting, which has been considered a likely feature of the K^+ buffering system (Somjen (2004)). A further increase in glial gap junctional coupling, however, leads to propagation failure. Thus, blocking gap junctions from this higher value of coupling results in an increased occurrence of SD, which is in agreement with the experimental observation that SD is induced more easily in mice whose glial gap junctions are inactivated (Theis et al (2003)).

The above is reminiscent of the effect of inter- or intracellular resistance on action potential propagation and initiation in cardiac and neuronal physiology. Reducing the intracellular (or intercellular, in the case of cardiac tissue) resistance leads not only to an increase in propagation speed but also to a higher threshold current for excitation (Keener and Sneyd (1998)) thus increasing the possibility for propagation failure. However, the role of glial gap junctional coupling here is more subtle, as the glia are not directly involved in the neuronal depolarization.

Timing of the DC shift The relative timing of the DC shift and the $[K^+]_e$ increase has been frequently studied, along with the timing of other changes, in an attempt to understand the mechanism of propagation (Herreras et al (2005)). In particular, the DC shift has often been observed to start earlier than the steep rise in $[K^+]_e$. This has been interpreted as an absence in the expected prodromal $[K^+]_e$ rise that should accompany the SD wave if SD propagates via extracellular ionic (electro)diffusion.

Comparing $[K^+]_e$ and extracellular voltage traces in Fig. 2 (c) and (e), we see that the steep $[K^+]_e$ rise is indeed preceded by a softer gradual negative DC shift. As seen in Fig 4a, this early DC shift is more prominent for greater values of the gap junctional coupling strength d. Note that this negative early DC shift was absent in the two-compartment simulation shown in Fig. 3. This led us to examine how the timing of the DC shift, the neuronal and glial depolarizations, and the $[K^+]_e$ increase are influenced by glial parameters.

The neuronal depolarization and $[K^+]_e$ increase occurred almost simultaneously for nearly all parameter values, as shown in Fig. 5a. Only when the gap

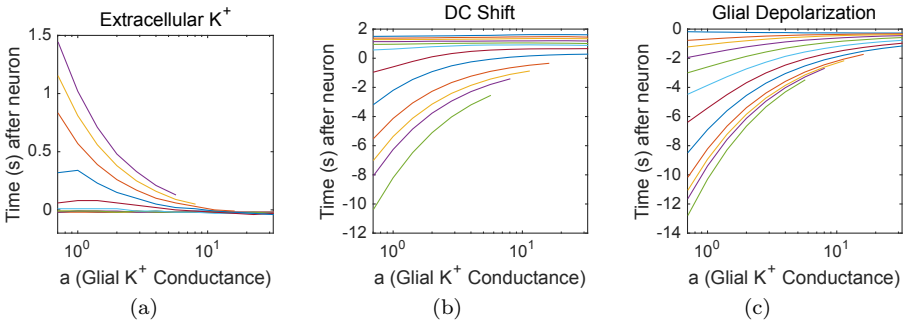

Fig. 5 Effects of glial gap junctional coupling and potassium conductance on the relative timing of the DC shift, extracellular potassium increase, and neuronal and glial depolarizations. The timing of a 1 mM change in the $[K^+]_e$ (a), a 2 mV change in the extracellular potential (DC shift) (b), and a 2 mV change in the glial membrane potential (c) are shown relative to a 2 mV change in the neuronal membrane potential. For (a), the highest line shows $d = 2$, with each lower line showing d equal to half the line above, and values between 2^{-4} and 0 nearly indistinguishable. In (b) and (c) the order is reversed, with the lowest line representing $d = 2$ and the highest line $d = 0$.

junction strength was high and the K^+ conductance low did the two changes separate, with the $[K^+]_e$ increase occurring after the neuronal depolarization by at most 1.5 seconds. This highlights the central role of extracellular K^+ in propagation of SD, with increased $[K^+]_e$ causing neuronal depolarization, which causes further release of K^+ in a feedback loop leading to SD.

The DC shift, however, sometimes occurred before and sometimes after the neuronal depolarization. Fig. 5b shows the timing of the DC shift relative to the neuronal depolarization. If the gap junction strength was low, at or below $d = 0.0625$, the DC shift occurred last, approximately one to two seconds behind the neuronal depolarization and $[K^+]_e$ increase. For intermediate values of the gap junction strength, $d = 0.125$ and $d = 0.25$, the DC shift occurred before the neuronal depolarization and $[K^+]_e$ increase by up to several seconds for low values of the K^+ conductance, and after by up to a second for high values. For high values of the gap junction strength, the DC shift occurred one to eight seconds before the neuronal depolarization, with greater differences for lower values of the K^+ conductance strength.

Fig. 5c shows the relative timing of the glial depolarization to the neuronal depolarization, revealing that the glial depolarization always occurred first, though the difference in timing was dependent on the parameters. When the gap junction strength was very low, the glial depolarization was less than a second before the neuronal depolarization. For intermediate values of the gap junction strength, the K^+ conductance began to affect the difference; low K^+ conductance results in glial depolarization occurring several seconds before neuronal depolarization and high K^+ conductance approximately one second before. At very high gap junction strength and low K^+ conductance, the glia began depolarizing over 10 seconds before the neuron. The glia depolarize earlier for higher values of d because of the electrotonic effect. With increased

gap junctional coupling, the glial depolarization spreads further from the SD wavefront. The significant difference in timing between glial and neuronal depolarizations for low glial K^+ conductance indicates that the depolarization of the glial cells has a relatively small effect on the propagation at these levels of conductance, evident also in the relatively small variation in propagation speed for low glial K^+ conductance. We also note that for high gap junctional coupling, the timing of the glial depolarization and DC shift show similar behavior as functions of the glial K^+ conductance, which further indicates a close tie between the glia and the DC shift.

In comparison, the simulation without a glial compartment had the $[K^+]_e$ increase 0.4 seconds before the neuronal depolarization, while the DC shift began 0.5 seconds after the neuronal depolarization. This much earlier increase of $[K^+]_e$ highlights the role of the glia as a K^+ buffer. The timing of the DC shift without glia is similar to that of simulations with low glial gap junctional coupling.

As discussed in Section 3.1, propagation of SD waves in our simulations are due primarily to extracellular ionic electrodiffusion, and are thus in line with the Grafstein hypothesis. We see, however, that DC shift can indeed take place before the rise in $[K^+]_e$ if the glial gap junctional coupling is high. This suggests that the seeming absence of an expected prodromal $[K^+]_e$ increase cannot be used as evidence against the Grafstein hypothesis or more generally of propagation hypotheses that rely on extracellular ionic electrodiffusion.

3.3 Na^+/K^+ ATPase

We varied the strength of the Na^+/K^+ ATPase, from 0.5 to 1.5 times the reference value with three values of the gap junction strength d, 0.125, 0.25, and 0.5. Note that the glial gap junction and K^+ channel are energetically passive whereas the Na^+/K^+ ATPase expends chemical energy. By varying the Na^+/K^+ ATPase strength we are varying the (thermodyanically) active properties of the glia (and neurons) as opposed to passive properties which were varied in the previous section. In one set of simulations, we changed the pump strength on both the neuronal and glial membranes, and in another we changed the strength only on the glial compartment. Since changing the strength of the Na^+/K^+ ATPase changes the rest values of the concentrations and voltages, we allowed the system to come to rest before adding the excitation used to trigger SD. The new rest states for the different strengths are shown in Table 3.

Speed In all cases, increasing the pump strength slowed down the propagation of SD, as shown in figure 6, and increasing the gap junction strength increased the speed. When Na^+/K^+ ATPase strength was reduced in both the neuronal and glial membranes, SD was triggered without any excitation for $b = 0.5$ and $b = 0.6$, resulting in an indeterminate propagation speed. These results mimic the effects of ouabain, which inhibits Na^+/K^+ ATPase and has been used as a

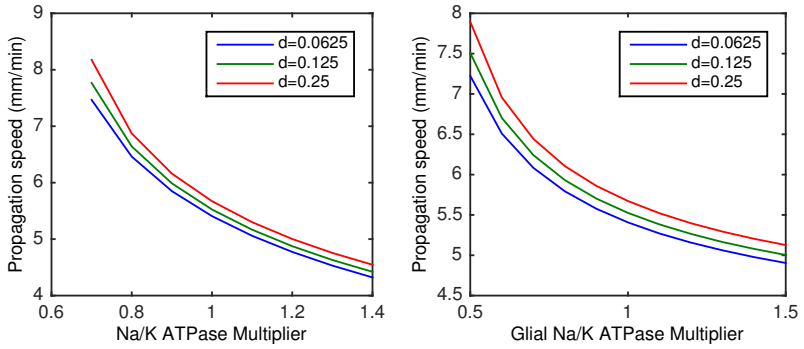

(a) (b)

Fig. 6 Effects of Na^+/K^+ ATPase on the propagation speed of SD, affecting both membranes (a) and only the glial membrane (b). Increasing the pump strength decreased the propagation speed in both cases.

trigger for SD in several experimental studies (Basarsky et al (1998); Charles and Brennan (2009); Dietz et al (2008)). When $b = 1.5$, our excitation protocol failed to trigger SD. In between those values, the propagation speed decreased with an increase in the pump strength, as shown in Fig. 6a.

With the pump strength only changed on the glial membrane (Fig. 6b), the propagation speed was 7.2–7.9 mm/min at $b = 0.5$ and decreased with increasing b to 4.9–5.1 mm/min when $b = 1.5$. Decreasing the glial pump strength reduces the membrane potentials in both neurons and glia and raises $[K^+]_e$, whose combined effect makes it easier to trigger SD at any point, resulting in an increase in propagation speed. Our simulations are consistent with the phenotype of a subtype of familial hemiplegic migraine (De Fusco et al (2003); Vanmolkot et al (2006)) in which mutations occur in the gene encoding the $\alpha 2$ subunit of the Na^+/K^+ ATPase whose expression is localized on glia (Cholet et al (2002)).

Timing of the DC shift The timing of the membrane depolarizations, DC shift, and $[K^+]_e$ increase, all measured relative to the rest state, was minimally affected by the Na^+/K^+ ATPase strength. The order of all events was determined by the gap junction strength, with only a slight increase in the amount of time between them as the Na^+/K^+ ATPase increased.

4 Conclusion

In this paper we performed a computational study of SD with a multi-compartmental model of neural tissue that incorporates ionic electrodiffusion and osmotic effects. This allowed us to compute the DC shift during SD and to perform a careful study of glial parameters on the properties of SD. We found that the speed of propagation, magnitude of the DC shift, and timing of the DC shift

and the $[K^+]_e$ rise vary greatly with glial parameters. Of particular interest are our results on the time-courses of the different biophysical variables. Grafstein's hypothesis and the role of $[K^+]_e$ in the propagation of SD has been a subject of much debate. In experiments, the DC shift is often seen prior to $[K^+]_e$ rise and on the basis of this, questions have been raised as to whether $[K^+]_e$ is indeed the propagating agent of SD. Our simulations show that the relative timing of the $[K^+]_e$ rise and the DC shift is highly dependent on glial parameters. On the other hand, a tight coupling of neuronal depolarization and $[K^+]_e$ rise is observed regardless of the value of the glial parameters. This strongly indicates the centrality of $[K^+]_e$ in SD propagation and argues against interpreting an early DC shift and an absence of an early $[K^+]_e$ rise as evidence against Grafstein's hypothesis. Furthermore, the dependence of the magnitude of the DC shift on the gap-junctional coupling of the glial cells, which serve as a K^+ buffer, indicates that the DC shift itself is intricately tied to $[K^+]_e$.

We found also that glial gap junctional coupling affected the speed of propagation and of propagation failure. Increasing gap junctional coupling leads to faster propagation speeds. This is, to the best of our knowledge, the first computational demonstration that the K^+ broadcasting hypothesis is theoretically feasible. On the other hand, higher values of gap junctional coupling can lead to propagation failure in agreement with experimental results reported in Theis et al (2003). Furthermore, the effects of channel strength on propagation speed suggest that propagation speed is not determined purely by diffusion, but also by how far the rest state is from the threshold for SD. In particular, we note that changes in the Na^+/K^+ ATPase strength caused as much variation in the propagation speed as glial gap-junctional coupling, despite the fact that these changes should have a much smaller impact on the effective diffusion coefficient. This may help to explain why experimental values for the propagation speeds cover a larger range than those seen in computational simulations.

One major limitation of this study is that the simulations are spatially one-dimensional. SD is known to propagate preferentially in dendritic layers (Somjen (2004)), and it is thus of interest to perform 2D simulations in which the extra dimension reflects the cortical layer structure. Such a model, for example, may help explain the contradictory experimental data on the effect of gap junctional coupling on SD (Martins-Ferreira and Ribeiro (1995); Nedergaard et al (1995); Tamura et al (2011); Theis et al (2003)). Our modeling framework is readily generalized to 2D or 3D, and this is an important direction for future study. We have recently succeeded in performing 2D computations, but the simulations are significantly more computationally intensive than the one-dimensional computations presented here (O'Connell (2016)). A considerable improvement on the nonlinear solver is likely necessary for detailed parameter studies that will allow for meaningful scientific exploration. In preliminary computations the annihilation and merging of two wave fronts have been seen, and more complicated wave patterns, such as spiral waves, are likely possible with appropriate initial data and parameter values. We have

also obtained computational indication that anisotropic glial gap junctional coupling may have subtle effects on SD propagation.

One important aspect of the model not used in this paper is the free-energy structure of the model, mentioned earlier and discussed in detail in Mori (2015). Indeed, SD can be thought of as a disruption in energy homeostasis of the cerebral cortex (Dreier et al (2013)), and our model offers a way to make such statements quantitative. We finally remark that the modeling framework used here and presented in Mori (2015) may be seen as a general coarse-grained model of electrophysiology at the tissue level, and is thus not limited in its application to SD. The modeling framework should find further applications in neurophysiology and beyond.

Appendix: Ion Channels

For each ion species i, we write the outward flux as the sum of transporters and ion channels, with h_i^k representing the combined effect of the Na^+/K^+ ATPase and any cotransporters, and m representing the different ion channels. Each channel is written as the product of the proportion of open channels $\hat{g}_i^{k,m}$ and a flux-voltage-concentration relationship $J_i^{k,m}$:

$$j_i^k = h_i^k + \sum_m \hat{g}_i^{k,m} J_i^{k,m},\ k = \mathrm{n}, \mathrm{g}.$$

For the flux-voltage-concentration relationship in some ion channels, we use the Nernst potential for ion i and cell type k,

$$E_i^k = \frac{RT}{z_i F} \ln\left(\frac{c_i^k}{c_i^{\mathrm{e}}}\right).$$

Persistent sodium current (neuron) Kager et al (2000); Yao et al (2011)

$$\begin{aligned}
\hat{g}_{\mathrm{Na}}^{\mathrm{n,P}} &= m^2 h \\
J_{\mathrm{Na}}^{\mathrm{n,P}} &= P_{\mathrm{Na}}^{\mathrm{n,P}} \frac{F\phi_{\mathrm{ne}}}{RT} \frac{c_{\mathrm{Na}}^{\mathrm{n}} \exp(\frac{F\phi_{\mathrm{ne}}}{RT}) - c_{\mathrm{Na}}^{\mathrm{e}}}{\exp(\frac{F\phi_{\mathrm{ne}}}{RT}) - 1} \\
\frac{dm}{dt} &= \alpha_m(1-m) - \beta_m m \\
\frac{dh}{dt} &= \alpha_h(1-h) - \beta_h h \\
\alpha_m &= \frac{1}{(1+\exp(-(0.143\phi_{\mathrm{ne}} + 5.67)))6} \\
\beta_m &= \frac{1}{(1+\exp(0.143\phi_{\mathrm{ne}} + 5.67))6} \\
\alpha_h &= 5.12 \times 10^{-6} \exp(-(0.056\phi_{\mathrm{ne}} + 2.94)) \\
\beta_h &= \frac{1.6 \times 10^{-4}}{1+\exp(-(0.2\phi_{\mathrm{ne}} + 8))}
\end{aligned}$$

Potassium delayed rectifier current (neuron) Kager et al (2000); Yao et al (2011)

$$\begin{aligned}
\hat{g}_{\mathrm{K}}^{\mathrm{n,DR}} &= m^2 \\
J_{\mathrm{K}}^{\mathrm{n,DR}} &= P_{\mathrm{K}}^{\mathrm{n,DR}} \frac{F\phi_{\mathrm{ne}}}{RT} \frac{c_{\mathrm{K}}^{\mathrm{n}} \exp(\frac{F\phi_{\mathrm{ne}}}{RT}) - c_{\mathrm{K}}^{\mathrm{e}}}{\exp(\frac{F\phi_{\mathrm{ne}}}{RT}) - 1} \\
\frac{dm}{dt} &= \alpha_m(1-m) - \beta_m m \\
\alpha_m &= \frac{0.016(\phi_{\mathrm{ne}} + 34.9)}{1 - \exp(-0.2(\phi_{\mathrm{ne}} + 34.9))} \\
\beta_m &= 0.25 \exp(-(0.025\phi_{\mathrm{ne}} + 1.25))
\end{aligned}$$

Transient potassium current (neuron) Kager et al (2000); Yao et al (2011)

$$\begin{aligned}
\hat{g}_{\mathrm{K}}^{\mathrm{n,A}} &= m^2 h \\
J_{\mathrm{K}}^{\mathrm{n,A}} &= P_{\mathrm{K}}^{\mathrm{n,A}} \frac{F\phi_{\mathrm{ne}}}{RT} \frac{c_{\mathrm{K}}^{\mathrm{n}} \exp(\frac{F\phi_{\mathrm{ne}}}{RT}) - c_{\mathrm{K}}^{\mathrm{e}}}{\exp(\frac{F\phi_{\mathrm{ne}}}{RT}) - 1} \\
\frac{dm}{dt} &= \alpha_m(1-m) - \beta_m m \\
\frac{dh}{dt} &= \alpha_h(1-h) - \beta_h h \\
\alpha_m &= \frac{0.02(\phi_{\mathrm{ne}} + 56.9)}{1 - \exp(-0.1(\phi_{\mathrm{ne}} + 56.9))} \\
\beta_m &= \frac{0.0175(\phi_{\mathrm{ne}} + 29.9)}{\exp(0.1(\phi_{\mathrm{ne}} + 29.9) - 1)} \\
\alpha_h &= 0.016 \exp(-(0.056\phi_{\mathrm{ne}} + 4.61)) \\
\beta_h &= \frac{0.5}{\exp(-(0.2\phi_{\mathrm{ne}} + 11.98)) + 1}
\end{aligned}$$

Potassium inward rectifier current (glia) Newman (1993); Steinberg et al (2005)

$$\begin{aligned}
\hat{g}_{\mathrm{K}}^{\mathrm{n,IR}} &= P_{\mathrm{K}}^{\mathrm{g,IR}} \sqrt{\frac{c_{\mathrm{K}}^{\mathrm{e}}}{3}} \frac{1 + \exp(18.5/42.5)}{1 + \exp((\phi_{\mathrm{ge}} - E_{\mathrm{K}}^{\mathrm{g}} + 18.5)/42.5)} \frac{1 + \exp((-118.6 - 85.2)/44.1)}{1 + \exp((-118.6 + \phi_{\mathrm{ge}})/44.1)} \\
J_{\mathrm{K}}^{\mathrm{n,IR}} &= F(\phi_{\mathrm{ge}} - E_{\mathrm{K}}^{g})
\end{aligned}$$

Leak currents (neuron, glia) Kager et al (2000); Yao et al (2011)

$$\begin{aligned}
\hat{g}_i^{k,\mathrm{L}} &= 1 \\
J_i^{k,\mathrm{L}} &= P_i^{k,\mathrm{L}} z_i F(\phi_{k\mathrm{e}} - E_i^k)
\end{aligned}$$

Na^+/K^+ ATPase current (neuron, glia) Yao et al (2011)

$$
\begin{aligned}
I_k^{\mathrm{ATP}} &= \frac{\bar{I}_k}{(1+m_{\mathrm{K}}/c_{\mathrm{K}}^{\mathrm{e}})^2(1+m_{\mathrm{Na}}/c_{\mathrm{Na}}^{k})^3} \\
h_{\mathrm{Na}}^{k,\mathrm{ATP}} &= 3I_k^{\mathrm{ATP}} \\
h_{\mathrm{K}}^{k,\mathrm{ATP}} &= -2I_k^{\mathrm{ATP}}
\end{aligned}
$$

Sodium, potassium, chloride cotransporter current (glia) Bennett et al (2008)

$$
\begin{aligned}
I_k^{\mathrm{NaKCl}} &= P^{\mathrm{NaKCl}} \ln\left(\frac{c_{\mathrm{Na}}^{\mathrm{g}} c_{\mathrm{K}}^{\mathrm{g}} (c_{\mathrm{Cl}}^{\mathrm{g}})^2}{c_{\mathrm{Na}}^{\mathrm{e}} c_{\mathrm{K}}^{\mathrm{e}} (c_{\mathrm{Cl}}^{\mathrm{e}})^2}\right) \\
h_{\mathrm{Na}}^{k,\mathrm{NaKCl}} &= I_k^{\mathrm{NaKCl}} \\
h_{\mathrm{K}}^{k,\mathrm{NaKCl}} &= I_k^{\mathrm{NaKCl}} \\
h_{\mathrm{Cl}}^{k,\mathrm{NaKCl}} &= 2I_k^{\mathrm{NaKCl}}
\end{aligned}
$$

Acknowledgements R.O. and Y.M. were supported by National Science Foundation Grant DMS 1516978. Y.M. thanks the Fields Institute (Toronto, Canada) for support during the spreading depression workshop in the summer of 2014. Many participants have given Y.M. valuable advice and encouragement.

References

Almeida ACG, Texeira HZ, Duarte MA, Infantosi AFC (2004) Modeling extracellular space electrodiffusion during Leão's spreading depression. IEEE T Bio-med Eng 51(3):450–458

Amzica F, Massimini M, Manfridi A (2002) Spatial buffering during slow and paroxysmal sleep oscillations in cortical networks of glial cells in vivo. J Neurosci 22(3):1042

Basarsky TA, Duffy SN, Andrew RD, MacVicar BA (1998) Imaging spreading depression and associated intracellular calcium waves in brain slices. J Neurosci 18(18):7189–7199

Bennett MR, Farnell L, Gibson WG (2008) A quantitative model of cortical spreading depression due to purinergic and gap-junction transmission in astrocyte networks. Biophysical Journal 95:5648–5660

Canals S, Marakova I, López-Aquado L, Largo C, Ibarz JM, Herreras O (2005) Longitudinal depolarization gradients along the somatadendritic axis of CA1 pyramidal cells: A novel feature of spreading depression. J Neurophysiol 94:943–951

Chang J, Brennan K, He D, Huang H, Miura R, Wilson P, Wylie J (2013) A mathematical model of the metabolic and perfusion effects on cortical spreading depression. PLoS One 8(8):e70,469, DOI 10.1371/journal.pone.0070469

Charles A, Brennan K (2009) Cortical spreading depression – new insights and persistent questions. Cephalalgia 29:1115–1124

Cholet N, Pellerin L, Magistretti P, Hamel E (2002) Similar perisynaptic glial localization for the na+, k+-atpase $\alpha 2$ subunit and the glutamate transporters glast and glt-1 in the rat somatosensory cortex. Cerebral Cortex 12(5):515–525

Dahlem M, Chronicle E (2004) A computational perspective on migraine aura. Prog Neurobiol 74(6):351–361

Dahlem M, Graf R, Strong A, Dreier J, Dahlem Y, Sieber M, Hanke W, Podoll K, Schöll E (2010) Two-dimensional wave patterns of spreading depolarization: Retracting, re-entrant, and stationary waves. Physica D 239(11):889–903

Dahlem MA, Hadjikhani N (2009) Migraine aura: retracting particle-like waves in weakly susceptible cortex. PLoS One 4(4):e5007

De Fusco M, Marconi R, Silvestri L, Atorino L, Rampoldi L, Morgante L, Ballabio A, Aridon P, Casari G (2003) Haploinsufficiency of atp1a2 encoding the na+/k+ pump $\alpha 2$ subunit associated with familial hemiplegic migraine type 2. Nat Genet 33(2):192–196

Dietz RM, Weiss JH, Shuttleworth CW (2008) Zn^{2+} influx is critical for some forms of spreading depression in brain slices influx is critical for some forms of spreading depression in brain slices. J Neurosci 28(32):8014–8024

Dreier J (2011) The role of spreading depression, spreading depolarization and spreading ischemia in neurological disease. Nat Med 17(4):439–447

Dreier JP, Reiffurth C (2015) The stroke-migraine depolarization continuum. Neuron 86(4):902–922

Dreier JP, Isele T, Reiffurth C, Offenhauser N, Kirov SA, Dahlem MA, Herreras O (2013) Is spreading depolarization characterized by an abrupt, massive release of gibbs free energy from the human brain cortex? The Neuroscientist 19(1):25–42

Gorji A, Scheller D, Straub H, Tegtmeier F, Köhling R, Höhling JM, Tuxhorn I, Ebner A, Wolf P, Panneck HW, Oppel F, Speckmann EJ (2001) Spreading depression in human neocortical slices. Brain Research 906:74–83

Grafstein B (1956) Mechanism of spreading cortical depression. J Neurophysiol 19(2):154–171

Hadjikhani N, del Rio MS, Wu O, Schwartz D, Bakker D, Fischl B, Kwong KK, Cutrer FM, Rosen BR, Tootell RB, Sorensen AG, Moskowitz MA (2001) Mechanisms of migraine aura revealed by functional MRI in human visual cortex. P Nat Acad Sci USA 98(8):4687–4692

Herreras O, Somjen GG (1993) Analysis of potential shifts associated with recurrent spreading depression and prolonged unstable spreading depression induced by microdialysis of elevated K^+ in hippocampus of anesthetized rats. Brain Research 610:283–294

Herreras O, Somjen G, Strong A (2005) Electrical prodromals of spreading depression void grafstein's potassium hypothesis. J Neurophysiol 94(5):3656–3657

Hille B, et al (2001) Ion channels of excitable membranes, vol 507. Sinauer Sunderland, MA

Kager H, Wadman WJ, Somjen GG (2000) Simulated seizures and spreading depression in a neuron model incorporating interstitial space and ion concentrations. J Neurophysiol 84:495–512

Keener JP, Sneyd J (1998) Mathematical physiology, vol 1. Springer

Largo C, Ibarz J, Herreras O (1997) Effects of the gliotoxin fluorocitrate on spreading depression and glial membrane potential in rat brain in situ. J Neurophysiol 78(1):295

Lashley KS (1941) Patterns of cerebral integration indicated by the scotomas of migraine. Arch Neuro Psychiatr 46(2):331

Lauritzen M, Dreier JP, Fabricius M, Hartings JA, Graf R, Strong AJ (2010) Clinical relevance of cortical spreading depression in neurological disorders: migraine, malignant stroke, subarachnoid and intracranial hemorrhage, and traumatic brain injury. J Cerebr Blood F Met 31(1):17–35

Leao AA (1944) Spreading depression of activity in the cerebral cortex. J Neurophysiol 7(6):359–390

Lehmenkühler A (1990) Spreading depression-reaktionen an der hirnrinde: Störungen des extrazellulären mikromilieus. EEG-EMG 21:1–6

Lehmenkühler A, Aitken P (1993) Migraine: Basic Mechanisms and Treatment:[Proceedings of the International Symposium Migraine, Basic Mechanisms and Treatment, Held in Münster (Germany) from March 8-11, 1992]. Urban & Schwarzenberg

Martins-Ferreira H, Ribeiro LJ (1995) Biphasic effects of gap-junctional uncoupling agents on the propagation of retinal spreading depression. Braz J Med Biol Res 28:991–994

Miura R, Huang H, Wylie J (2007) Cortical spreading depression: An enigma. Eur Phys J-Spec Top 147:287–302

Mori Y (2015) A multidomain model for ionic electrodiffusion and osmosis with an application to cortical spreading depression. Physica D 308:94–108

Nedergaard M, Cooper AJL, Goldman SA (1995) Gap junctions are required for the propagation of spreading depression. J Neurobiol 28(4):433–444

Newman EA (1993) Inward-rectifying potassium channels in retinal glial (muller) cells. The Journal of neuroscience 13(8):3333–3345

Nicholson C (1993) Volume transmission and the propagation of spreading depression. Migraine: Basic Mechanisms and Treatment pp 293–308

O'Connell RA (2016) A computational study of cortical spreading depression. PhD thesis, University of Minnesota

Pietrobon D, Moskowitz MA (2014) Chaos and commotion in the wake of cortical spreading depression and spreading depolarizations. Nat Rev Neurosci 15(6):379–393

Revett K, Ruppin E, Goodall S, Reggia J (1998) Spreading depression in focal ischemia: A computational study. J Cerebr Blood F Met 18(9):998–1007

Richter F, Lehmenkühler A (2008) Cortical spreading depression (csd): Ein neurophysiologisches korrelat der migräneaura. Der Schmerz 22:544–550

Shapiro BE (2000) An electrophysiological model of gap-junction mediated cortical spreading depression including osmotic volume changes. PhD thesis, UNIVERSITY OF CALIFORNIA Los Angeles

Shapiro BE (2001) Osmotic forces and gap junctions in spreading depression: A computational model. J Comput Neurosci 10:99–120

Somjen GG (1973) Electrogenesis of sustained potentials. Prog Neurobiol 1:199–237

Somjen GG (2004) Ions in the Brain. Oxford University Press

Steinberg B, Wang Y, Huang H, Miura R (2005) Spatial buffering mechanism: Mathematical model and computer simulations. Math Biosci Eng 2:675–702

Sugaya E, Takato M, Noda Y (1975) Neuronal and glial activity during spreading depression in cerebral cortex of cat. J Neurophysiol 38:822–841

Tamura K, Alessandri B, Heimann A, Kempski O (2011) The effect of a gap-junction blocker, carbenoxolone, on ischemic brain injury and cortical spreading depression. Neuroscience 194:262–271

Tfelt-Hansen P (2009) History of migraine with aura and cortical spreading depression from 1941 and onwards. Cephalalgia

Theis M, Jauch R, Zhuo L, Speidel D, Wallraff A, Döring B, Frisch C, Söhl G, Teubner B, Euwens C, Huston J, Steinhäuser C, Messing A, Heinemann U, Willecke K (2003) Accelerated hippocampal spreading depression and enhanced locomotory activity in mice with astrocyte-directed inactivation of connexin43. J Neurosci 23(3):766–776

Tuckwell HC (1981) Simplified reaction-diffusion equations for potassium and calcium ion concentrations during spreading cortical depression. Int J Neurosci 12(2):95–107

Tuckwell HC, Miura RM (1978) A mathematical model of spreading cortical depression. Biophys J 23:257–276

Vanmolkot KR, Kors EE, Turk U, Turkdogan D, Keyser A, Broos LA, Kia SK, van den Heuvel JJ, Black DF, Haan J, et al (2006) Two de novo mutations in the na, k-atpase gene atp1a2 associated with pure familial hemiplegic migraine. Eur J Hum Gen 14(5):555–560

Yao W, Huang H, Miura RM (2011) A continuum neuronal model for the instigation and propagation of cortical spreading depression. B Math Biol 73:2773–2790

Zandt BJ, ten Haken B, van Putten MJ, Dahlem MA (2015) How does spreading depression spread? physiology and modeling. Rev Neuroscience 26(2):183–198